Sensors & Actuators: B. Chemical 418 (2024) 136282

Contents lists available at ScienceDirect

Sensors and Actuators: B. Chemical

journal homepage: www.elsevier.com/locate/snb

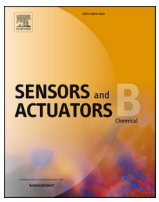

Nanoscopic catalyst-loaded porous metal oxide hollow frameworks using porous block copolymer templates for high performance formaldehyde sensors

Won-Tae Koo [a,1], Sungyoon Woo [a,1], Euichul Shin [a], Juyoung Lee [b], Hyunji Lee [c,d], Kang Hee Ku [b,*], Sang-Joon Kim [c,d,**], Il-Doo Kim [a,*]

[a] Department of Materials Science and Engineering, Korea Advanced Institute of Science and Technology (KAIST), Daejeon 34134, Republic of Korea
[b] School of Energy and Chemical Engineering, Ulsan National Institute of Science and Technology (UNIST), Ulsan 44919, Republic of Korea
[c] Center for CO2 & Energy, Korea Research Institute of Chemical Technology (KRICT), 141 Gajeong-ro, Daejeon 34114, South Korea
[d] Department of Advanced Materials and Chemical Engineering, University of Science and Technology (UST), Daejeon 34114, Republic of Korea

ARTICLE INFO

Keywords:
Porous metal oxides
Porous microparticles
Block copolymers
Hollow frameworks
Catalysts
Chemical sensors

ABSTRACT

Porous and hollow nanostructures functionalized with nanoscopic catalysts have attracted considerable interest in a wide range of applications depending on surface reactions. In this study, we present an efficient and versatile synthetic strategy of porous metal oxide hollow frameworks (HFs) decorated with noble metal nanoparticles (NPs). The key lies in the use of porous and bicontinuous polystyrene-*block*-poly(4-vinylpyridine) (PS-*b*-P4VP) microparticles as templates, which feature pores on the order of several hundred nanometers in size. Homogeneous Pt loading on the surface of the porous microparticles is achieved through the preferential adsorption of Pt precursors onto the P4VP block via electrostatic interactions. Subsequent SnO_2 thin film deposition and calcination ultimately yield honeycomb-like SnO_2 HFs with macropores and uniform distribution of Pt NPs. The Pt NP-loaded SnO_2 HFs exhibit exceptional formaldehyde (HCHO) sensing capabilities, characterized by remarkable sensitivity (31.4 at 5 ppm), rapid response time (4.7 s at 5 ppm), ultra-low detection limit of 10 ppb, and remarkable cross-selectivity. These outstanding features result from their high surface area, gas permeability within porous hollow structures, and well-dispersed Pt NPs, which catalytically activate the sensor. Our study provides great promise for advancing surface catalytic reactions due to their exceptional surface area and gas permeability, paving the way for future applications.

1. Introduction

Chemiresistive sensors, which can detect gas molecules by monitoring the changes in electrical resistances arising from surface chemical reactions, have garnered significant attention across various fields, including the detection of hazardous gases [1], analysis of exhaled breath constituents [2], environmental monitoring and regulation [3,4], and the evaluation of food product quality [5]. Nevertheless, chemiresistive sensors encounter formidable challenges, particularly limited responsiveness, and insufficient selectivity [6,7]. As surface reactions on these sensors can be triggered by a variety of gas molecules, selective initiation of surface reactions specific to a target gas becomes imperative. Furthermore, the enhancement of surface reactions is required to improve overall sensing characteristics.

To address these challenges, the utilization of nanomaterials containing noble metal nanoparticles (NPs) has emerged as a compelling and effective solution among various methodologies. This preference primarily arises from the substantial surface area provided by nanostructured materials and their inherent potential for catalytic activation [8–10]. Extensive reports cover a diverse spectrum of nanomaterials, including zero-dimensional (i.e., particles and clusters) [11,12], one-dimensional (i.e., nanofibers, nanowires, or nanorods) [13,14], two-dimensional (i.e., nanosheets or nanoflakes) [15], as well as three-dimensional structures with heterogeneous or hierarchical

* Corresponding authors.
** Corresponding author at: Center for CO2 & Energy, Korea Research Institute of Chemical Technology (KRICT), 141 Gajeong-ro, Daejeon 34114, South Korea.
E-mail addresses: kangheeku@unist.ac.kr (K.H. Ku), sangjoon@krict.re.kr (S.-J. Kim), idkim@kaist.ac.kr (I.-D. Kim).
[1] These authors contributed equally to this work.

https://doi.org/10.1016/j.snb.2024.136282
Received 27 March 2024; Received in revised form 7 July 2024; Accepted 9 July 2024
Available online 10 July 2024

configurations [16]. In addition, when considering the infiltration of gas molecules across entire sensing layers, porous and hollow frameworks are exceptional sensing platforms due to their enhanced gas permeability and substantial surface areas [17,18]. To date, numerous efforts have been devoted to preparing porous and hollow nanomaterials decorated with noble metal NPs [10,19]. However, existing methods for decorating these materials with noble metal NPs often involve multiple, time-consuming steps. The main challenge is the simultaneous synthesis of porous hollow structures and metal NPs, which leads to process complexity. Therefore, there is a compelling need for an efficient methodology tailored to create catalyst-incorporated porous and hollow nanostructures while ensuring highly uniform distribution and the preservation of well-defined nanostructures.

Block copolymer (BCP) particles offer precise control over nanostructure organization, overall shape, surface structure, and versatile functionalization. Therefore, they are promising candidates as sacrificial hard templates for crafting metal NP-loaded metal oxide nanostructures [20–22]. BCPs featuring various functional groups such as amines, carboxyls, and thiols, have been employed to introduce various catalysts into the desired location by infiltrating metallic precursors and subsequently reducing them to form metallic NPs [23–25]. Recently, the self-assembly of amphiphilic BCPs from the solvent-evaporative emulsion droplet has proven highly effective in generating bicontinuous porous microparticles with high surface area [26–28]. From these results, we envisioned a straightforward method for producing porous metal oxide hollow frameworks, uniformly functionalized with nanoscopic catalysts, leveraging BCP microparticles with a porous architecture.

In this work, we introduce an innovative synthetic approach for the fabrication of porous SnO_2 hollow frameworks (HFs) decorated with catalytic platinum (Pt) NPs, specifically designed for formaldehyde (HCHO) sensing. This method leverages sacrificial templates consisting of uniform Pt-functionalized porous polystyrene-*block*-poly(4-vinyl pyridine) (PS-*b*-P4VP) microparticles. Pt precursors were evenly distributed over the P4VP block, followed by the deposition of SnO_2 and subsequent calcination, resulting in the macro-meso porous honeycomb hemisphere-shaped Pt NP-loaded metal oxide HFs (Pt/SnO_2 HFs). The Pt/SnO_2 HFs exhibited exceptional HCHO sensing properties, characterized by a robust response (31.4 at 5 ppm), superior sensitivity (10 ppb), rapid response time (4.7 s at 5 ppm), and remarkable cross-selectivity. These sensing results are attributed to the inherent porous metal oxide hollow structure and the catalytic activation of Pt NPs.

2. Experimental section

2.1. Materials

Sodium dodecyl sulfate (SDS, molecular weight [M_W] = 288.38, ≥ 97 %), chloroplatinic acid hydrate ($H_2PtCl_6{\cdot}6\ H_2O$, M_W 517.90, ≥ 37.50 % Pt basis), and toluene (≥ 99.5 %) were purchased from Sigma-Aldrich. Polystyrene-*block*-poly(4-vinylpyridine) (PS_{109k}-*b*-$P4VP_{27k}$) copolymer (number-average molecular weights (M_n) = 136 kg mol^{-1}, dispersity ($Đ$) = 1.12) was purchased from Polymer Sources Inc. We purchased all sample gases (purity 99.99 %) from commercial sources (Samoh Gas Co., Daejeon, Korea). All chemicals were used as received without further purification.

2.2. Synthesis of Pt/SnO_2 HFs

A schematic illustration of the overall process for synthesizing Pt/SnO_2 HFs is summarized in Fig. S1. A toluene solution containing 10 mg mL^{-1} of PS-*b*-P4VP (4 mL) was emulsified in a continuous phase of SDS solution (0.4 wt%, 80 mL) by using a Shirasu porous glass (SPG) membrane device [29,30]. A membrane with a pore size of 1.1 μm was used to produce monodisperse emulsion droplets. Subsequent toluene evaporation at room temperature over 24 h resulted in the formation of porous PS-*b*-P4VP particles. After repeated centrifugation to remove the residual surfactants, a Pt precursor solution was added to the particle suspension in a 1:1 molar ratio relative to the P4VP unit. The mixture was stirred at room temperature for 24 h and purified by washing with deionized water and repeated centrifugations. These Pt-BCP particles were transferred onto Si wafer substrates using a dipping method. After drying the Pt-BCP-coated Si wafer substrate in a vacuum open at 80 °C for 4 h, we used radio frequency magnetron sputtering to deposit SnO_2 in a thickness ranging from 30 to 90 nm. The sputtering process was conducted at a working pressure and power of 1×10^{-2} atm and 20 W, respectively, while maintaining a deposition temperature at room temperature. The sputter-deposition times were controlled at 3, 6, and 9 min to optimize Pt-BCP/SnO_2 particles. The substrate was rotated during this process to ensure uniform deposition. Lastly, the calcination of Pt-BCP/SnO_2 particles at 600 °C for 1 h in a box furnace produced Pt/SnO_2 HFs. The pristine SnO_2 HFs as a control sample were prepared using the same process, excluding the Pt infiltration step.

2.3. Characterizations

The microstructures of materials were investigated by using field-emission scanning electron microscopy (SEM) (FE-SEM, Nova 230) with an acceleration voltage of 10 keV. The transmission electron microscopy (TEM) images, selected area diffraction (SAED) patterns, and Energy-dispersive spectrometry (EDS) mapping images were obtained by Tecnai F30 S-Twin (FEI) and JEM-2100 F (JEOL) with 300 keV and 200 keV electrons, respectively. The crystal structures were investigated by the X-ray diffraction (XRD) analysis (SmartLab, Rigaku) with Cu Kα sources (λ = 1.5418 Å). To analyze Pt NPs, we carried out double-aberration-corrected TEM analysis (Titan cubed G2 60–300, FEI). We also conducted X-ray photoelectron spectroscopy (XPS) analysis (Thermo VG Scientific) to verify the chemical state of Pt NPs with a beam size of 0.4 mm and high vacuum condition of 10^{-8}~10^{-9} mbar.

2.4. Gas sensing measurements

HCHO sensing tests were carried out using a homemade testing system described in the previous report [4]. An alumina (Al_2O_3) substrate with an area of 2.5 mm × 2.5 mm and a thickness of 0.2 mm was prepared. Gold (Au) electrodes with a distance of 75 μm were patterned on Al_2O_3 substrates. We deposited sensing materials by the drop-coating method. Firstly, samples (6 mg) dispersed in ethanol (300 mL) were sonicated for 10 min. Then, 5 μL of the suspension was drop-coated on the Al_2O_3 substrates three times with a heating temperature of 60 °C. Sensing tests were conducted in a sealed chamber at operating temperatures of 400 °C under dry air. The operating temperature was controlled through Joule heating of Pt electrodes patterned on the backside of the sensor substrates. Sensors were exposed to a target gas for 10 min and subsequently to air for 10 min, with the real-time monitoring of sensor resistances (34972 A, Agilent). The concentrations of gases were controlled by the mixing ratio of fresh air and sample gases with the aid of mass flow controllers. For instance, to investigate sensing properties to 5 ppm of HCHO, the flow ratio of the fresh air and HCHO samples (20 ppm in an N_2 balance) was controlled to 3:1, thus diluted HCHO gases (5 ppm) with the air were injected into the gas sensing test chamber. The sample gases, containing analytes such as acetone, hydrogen sulfide, toluene, methane, ammonia, nitric oxide, and xylene, were also prepared at a concentration of 20 ppm in an N_2 balance. The gas concentration was modulated using the same method. Responses of sensors are defined by the following equation, (R_{air}/R_{gas}), where R_{air} is the baseline resistance exposed to air and R_{gas} is the resistance when exposed to gas molecules.

3. Results and discussion

The synthesis of Pt/SnO_2 HFs begins with the fabrication of Pt

precursor-loaded PS-*b*-P4VP (Pt-BCP) particles, serving as a template, as depicted in Fig. 1**a**. First, the porous microparticles were produced by utilizing cross-flow membrane emulsification with a tubular SPG membrane, a well-established method renowned for its suitability in the large-scale production of uniformly sized BCP particles [29,30]. A toluene solution of PS_{109k}-*b*-$P4VP_{27k}$ was pressurized and passed through the SPG membrane, into an aqueous solution of SDS surfactant with a concentration of 0.4 wt%. The emulsions were generated through the shear force exerted by the stirrer in the continuous phase, with SDS promptly adsorbing at the interface of these emulsions. In particular, the cooperative co-adsorption between PS-*b*-P4VP and SDS at the emulsion interface leads to the remarkable reduction of the interfacial tension, resulting in the roughening of the emulsion interface [27,30]. Subsequent infiltrations of surrounding water into the emulsion triggered by continuous evaporation of toluene produced the porous particles with a bicontinuous BCP framework. The use of a 1.1 μm membrane resulted in the production of porous particles with an average diameter of 1.25 ± 0.11 μm, which exhibited a narrow size distribution with a coefficient of variation within 10 % (Fig. S2). The particles exhibited a porous structure both on the surface and inside, with a pore size of 200–400 nm (Fig. 1**b**). This structure comprised a continuous PS framework with collapsed P4VP chains on the surface of the porous structure. Additionally, Pt precursors were introduced onto the pore surface of the porous PS-*b*-P4VP particles, facilitated by the strong electrostatic attraction between the Pt precursor ($PtCl_6^{2-}$) and the protonated P4VP chain. The SEM and TEM images in Figs. 1**b and** 1**c** show the detailed structural transformations. Notably, during the infiltration of Pt precursors, the porous structure retained its stability without any deformation. For a more reliable Pt analysis, high-angle annular dark-field scanning TEM (HAADF-STEM) and EDS were performed, as depicted in Fig. 1**c**. After selectively staining the P4VP chains in the Pt-BCP particles with iodine vapor, the distribution of carbon (C), Pt, and iodine (I) elements was tracked to capture the spatial arrangement of Pt ions. The EDS image confirms the homogeneous distribution of Pt within the Pt-BCP particles. Subsequently, the synthesized low-density Pt-BCP particles were dispersed into deionized water where they floated due to their lower density, leading to natural agglomeration resulting from surface tension reduction. This process resulted in the formation of a monolayer consisting of these particles on the substrate via a simple dipping method illustrated in Fig. S3.

In the next step, SnO_2 was sputtered onto the Pt-BCP particles, resulting in the formation of Pt-BCP/SnO_2 composite particles (Fig. 2**a**). Due to the straightness deposition of the sputtering in vertical direction, Pt precursors in Pt-BCP/SnO_2 particles were situated beneath the SnO_2 layers. For the deposition of SnO_2 thin films on the Pt-BCP particles, we optimized the sputtering times at 3 min (Fig. 2**a-i**), 6 min (Fig. 2**a-ii**), and 9 min (Fig. 2**a-iii**) to regulate the thickness of the SnO_2 thin films adhering to the Pt-BCP particles. This optimization is crucial to ensure structural stability and maintain a porous framework during post-calcination. Excessively thin coatings lead to structural instability and challenges in maintaining the structure, whereas overly thick coatings risk pore blockage after calcination (Fig. S4). Under the optimal sputtering conditions (6 min), the deposition of the SnO_2 thin film resulted in a modest reduction in the average pore size, from 300 nm (see Fig. 1**b**) for Pt-BCP particles to 150 nm for Pt-BCP/SnO_2 particles (Fig. 2**a-ii**). This change is mainly due to the step coverage effect inherent in physical vapor deposition processes. Finally, calcination of the Pt-BCP/SnO_2 particles at 600 °C for 1 h not only removes the polymers within the composites but also activates the Pt precursors into Pt NPs. In addition, the step coverage regions generated during the sputtering of SnO_2 thin films were transformed into large pores during the calcination process due to the presence of voids or relatively thin regions in the sidewalls of pores in Pt-BCP/SnO_2 particles, thereby resulting in the formation of honeycomb-shaped hemispheres (Fig. 2**b**). Therefore, the complete removal of the PS-*b*-P4VP particle template within the composites resulted in the formation of honeycomb hemispherical hollow SnO_2 structures with Pt NPs anchored inside the hollow framework (Fig. 2**b-i**). The STEM image of Pt/SnO_2 HFs clearly showed the highly porous and hollow structures of Pt/SnO_2 HFs (Fig. 2**b-ii**). In addition, the Pt-BCP/SnO_2 particles that had initially formed a monolayer on the substrate

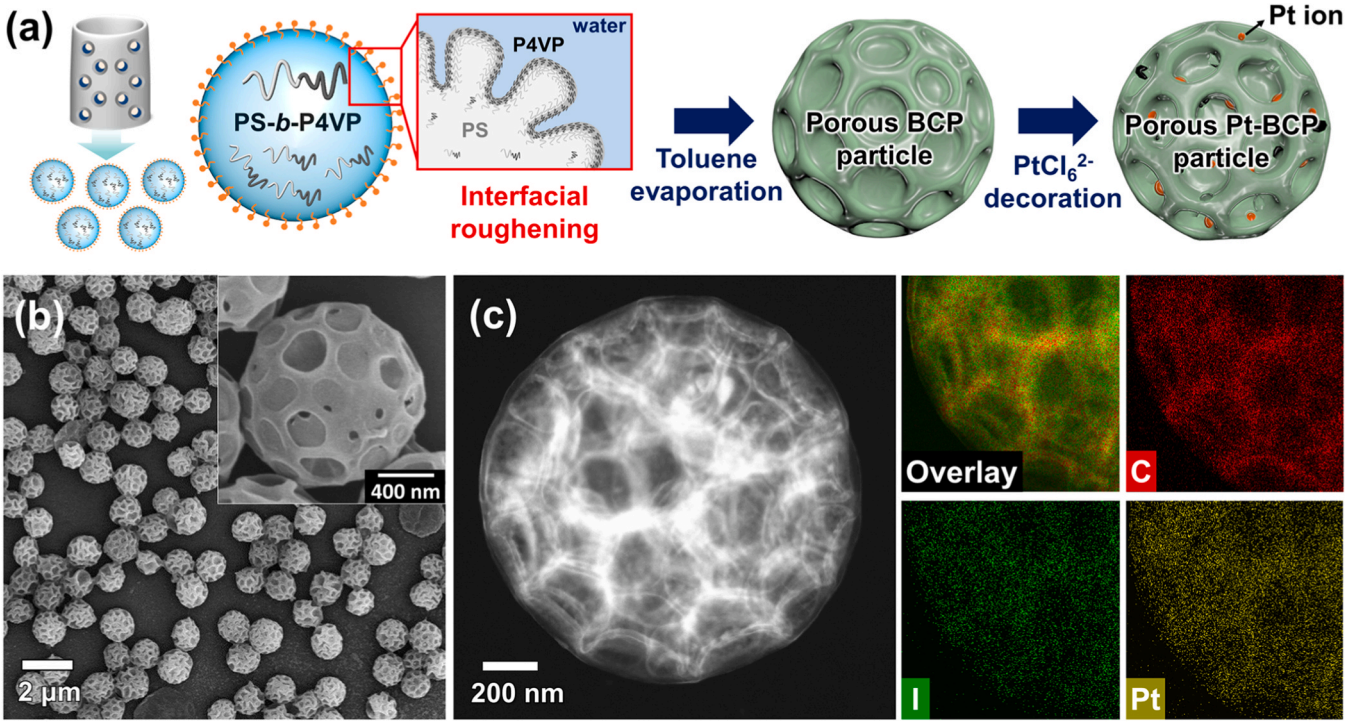

Fig. 1. Fabrication of Pt-decorated porous BCP microparticles. (a) Schematic illustration of the production of porous PS-*b*-P4VP microparticles functionalized with Pt precursors (referred to as Pt-BCP) from toluene-in-water emulsion. (b) SEM and (c) HAADF-STEM images along with EDS mapping for carbon (C), iodine (I), and platinum (Pt) of the porous Pt-BCP particles. Iodine vapor was used for the selective staining of the P4VP domain.

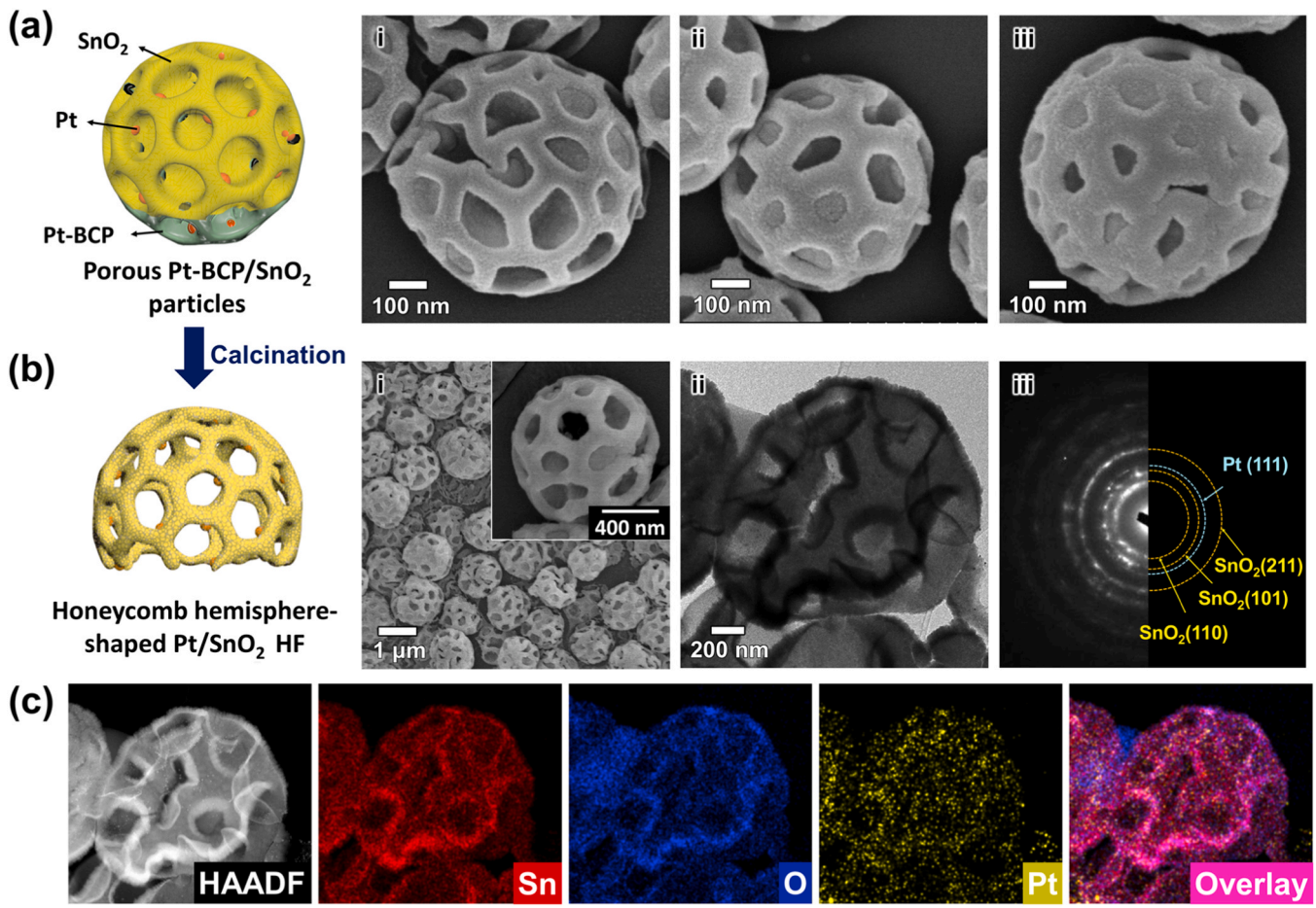

Fig. 2. Structural evolution of Pt/SnO_2 HFs. (a) Schematic illustration and corresponding SEM images of Pt-BCP/SnO_2 particles with different SnO_2 sputtering times of (a-i) 3 min, (a-ii) 6 min, and (a-iii) 9 min. In the schematic, Pt is shown on the surface of Pt-BCP/SnO_2 for illustrative purposes. However, in reality, Pt is positioned beneath the SnO_2 layers due to the vertical deposition of the sputtering method. (b) Schematic illustration of Pt/SnO_2 HFs with SEM and TEM analysis: (b-i) SEM images, (b-ii) TEM image, and (b-iii) SAED patterns of Pt/SnO_2 HFs. (d) HAADF-STEM images of Pt/SnO_2 HFs with EDS elemental mapping of Sn, O, Pt, and overlayer. Pt NPs are anchored inside the hollow framework.

maintained their aligned monolayer structure even after the sintering process, despite the removal of BCP (Fig. S5). Despite variations in pore shapes due to the roughness of SnO_2 films, this process increased the average pore size from 150 nm in Pt-BCP/SnO_2 particles to 200 nm in Pt/SnO_2 HFs. This increase in pore size is attributed to the degradation of the polymeric component. Although some particles showed slight collapse, the majority retained their porous and hollow configurations, therefore SnO_2 HFs are formed in a very thin shell. The SAED pattern analysis showed the crystalline nature of SnO_2 and Pt within the Pt/SnO_2 HFs (Fig. 2**b-iii**). In addition, XRD analysis of Pt/SnO_2 HFs also confirmed the polycrystalline structures of Pt/SnO_2 HFs (Fig. S6). In addition, the EDS elemental analysis exhibited the homogeneous distribution of Pt elements within Pt/SnO_2 HFs (Fig. 2**c**).

To demonstrate the presence of Pt NPs in Pt/SnO_2 HFs, we further carried out high-resolution TEM and XPS analysis. The double abbreviation-corrected HAADF-STEM image of a single Pt/SnO_2 HF showed numerous brighter points (Pt NPs) on the hollow and porous structures (SnO_2 HF) (Fig. 3**a**), demonstrating that Pt NPs were well-distributed on the surface of Pt/SnO_2 HFs. The size of Pt NPs is identified as 2–9 nm, with an average size of 5.8 nm (Fig. S7). In addition, the high-resolution TEM image of Pt/SnO_2 HFs revealed the co-existence of lattice planes corresponding to SnO_2 (110), SnO_2 (101), and Pt (111) (Fig. 3**b**). Moreover, the HAADF-STEM image under high magnification (Fig. 3**c**) and its corresponding EDS elemental mapping images (Fig. 3**d**) clearly showed the Pt NPs on SnO_2 HFs. We further investigated the chemical states of Pt NPs using XPS analysis. First of all, we verified SnO_2 peaks in the XPS analysis. The XPS analysis of Pt/SnO_2 HFs in the vicinity of Sn 3d peaks showed two characteristic peaks of $3d_{5/2}$ and $3d_{3/2}$ and at the binding energies of 486.7 and 495.1 eV and, respectively (Fig. 3**e**). These peak positions indicated the oxidation of Sn (Sn^{4+}) [31]. However, the Pt 4 f peaks in XPS analysis exhibited the majority of Pt^0 with peak values at 71.0 eV for $4f_{7/2}$ and 74.3 eV for $4f_{5/2}$ and, with minority of Pt^{2+} peaks (71.9 eV for $4f_{7/2}$ and 75.2 eV for $4f_{5/2}$) and Pt $^{4+}$ peaks (74.7 eV for $4f_{7/2}$ and 76.8 eV for $4f_{5/2}$) [32]. These XPS results clearly confirmed the functionalization of Pt NPs in the SnO_2 matrix. It is noted that the minority peaks of Pt^{2+} and Pt^{4+} observed in Pt NPs are attributed to the surface oxidation of Pt NPs. Since Pt NPs have high surface energy and reactivity, Pt NPs are partially oxidized during the annealing process for the preparation of Pt/SnO_2 HFs [33,34].

To highlight the robust catalytic activity of Pt/SnO_2 HFs and their potential application in highly sensitive and selective gas sensors, we investigated their chemiresistive properties for HCHO sensing. HCHO is recognized as one of the noxious and hazardous gases, with even parts per million (ppm) levels of inhalation posing a severe risk of respiratory ailments [35]. Therefore, there is an urgent need for the rapid detection of HCHO to ensure safety. We engineered chemiresistive sensors using Pt/SnO_2 HFs with varying Pt NP loadings at concentrations of 0.05 wt%, 0.10 wt%, 0.25 wt%, and 0.50 wt%, denoted as Pt(0.05)/SnO_2 HFs, Pt(0.10)/SnO_2 HFs, Pt(0.25)/SnO_2 HFs, and Pt(0.50)/SnO_2 HFs, respectively. The gas sensing tests were conducted by the homemade testing system (Fig. S8). Details are described in the Experimental section.

Fig. 4**a** presents the synthetic process of sensors based on Pt/SnO_2

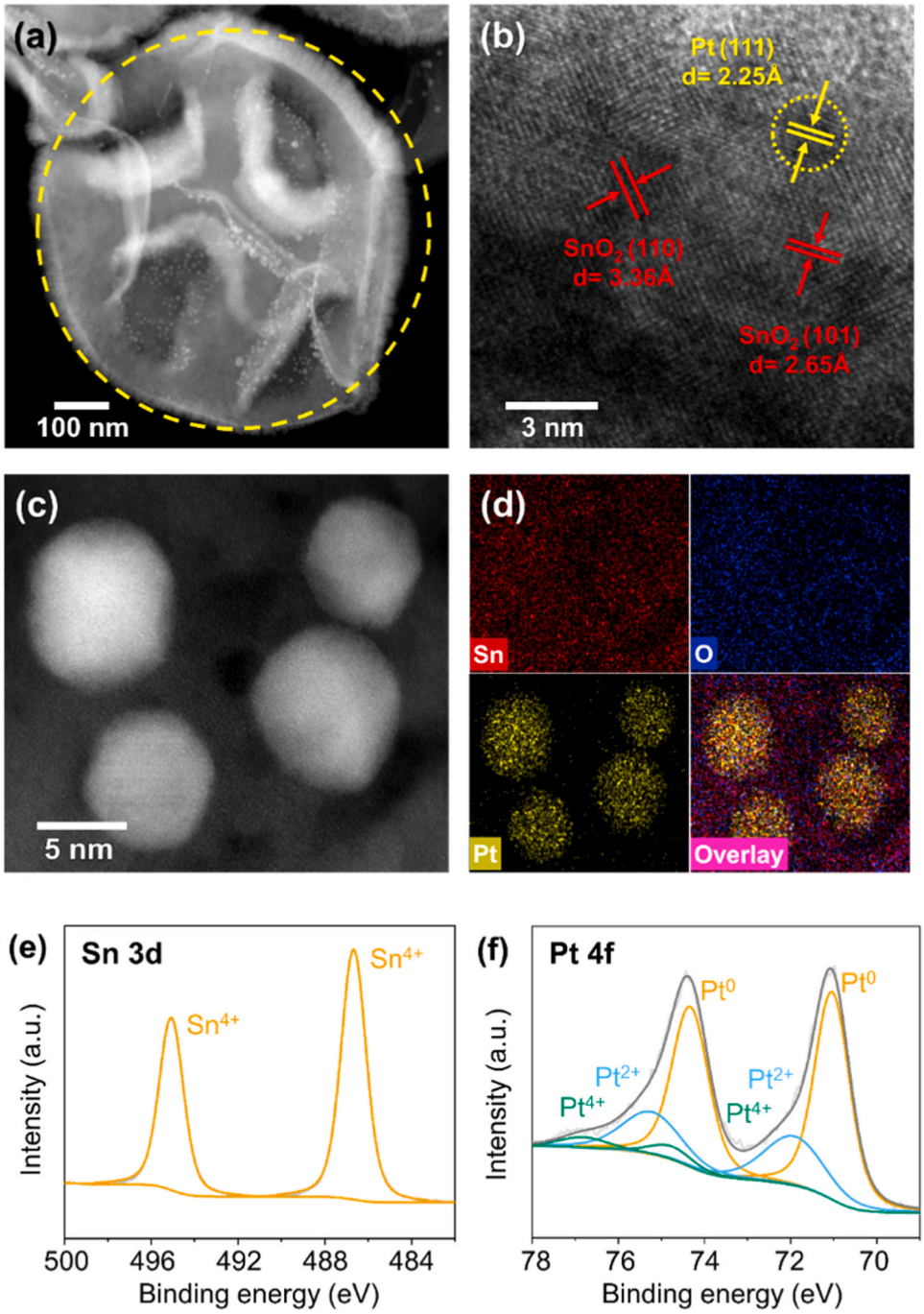

Fig. 3. Analysis of Pt NPs within Pt/SnO_2 HFs. (a) HR-TEM and (b) HAADF-STEM images of Pt/SnO_2 HFs. (c) HAADF-STEM image of Pt/SnO_2 HFs under high magnification. (d) EDS elemental mapping images for Sn, O, Pt, and all elements. XPS spectra of Pt/SnO_2 HFs in the vicinity of (e) Sn 3d and (f) Pt 4 f.

HFs, which function as the sensing layer for the detection of HCHO. The Pt/SnO_2 HFs prepared by the same synthetic method discussed above were drop-coated on the sensor substrate patterned by two parallel Au electrodes. A comprehensive, step-by-step procedure is available in Fig. S1 and the Experimental section. Fig. 4**b** shows the dynamic response transitions of pristine SnO_2 HFs and Pt/SnO_2 HFs when exposed to 1–5 ppm HCHO molecules. The baseline resistances were 2.4 MΩ for pristine SnO_2 HFs, 31 MΩ for Pt(0.05)/SnO_2 HFs, 40 MΩ for Pt(0.10)/SnO_2 HFs, 27 MΩ for Pt(0.25)/SnO_2 HFs and 17 MΩ for Pt (0.50)/SnO_2 HFs) (Fig. S9). Then, the sensor response was defined as R_{air}/R_{HCHO}, where R_{air} and R_{HCHO} are the sensor resistances in response to fresh air and HCHO molecules, respectively. Among Pt/SnO_2 HFs with different Pt loading amounts, Pt(0.10)/SnO_2 HFs showed the highest HCHO sensing responses (31.4 at 5 ppm) than other samples (16.8 for Pt (0.05)/SnO_2 HFs, 7.2 for Pt(0.25)/SnO_2 HFs and 13.5 for Pt(0.50)/SnO_2 HFs). Therefore, the optimal condition of Pt loading is 0.1 wt%, and the Pt(0.10)/SnO_2 HFs showed a 3.18-fold higher response (31.4 at 5 ppm) compared to pure SnO_2 HFs (10.1 at 5 ppm). It is noted that the optimum catalyst loading amounts (Pt 0.10 wt%) is explained by the relationship between the catalytic activation of Pt NPs and the surface reactions on SnO_2. Ultra-low concentrations of Pt NPs are not sufficient for catalytic activation, whereas excessive catalyst loading leads to the aggregation of Pt NPs during the calcination. For instance, excessively high Pt concentrations increase the size of Pt NPs from 5.8 nm (0.1 wt%) to 20 nm (0.5 wt%) (Fig. S10). These aggregations not only decrease the reactivity of the catalyst itself but also block the surface reaction sites on

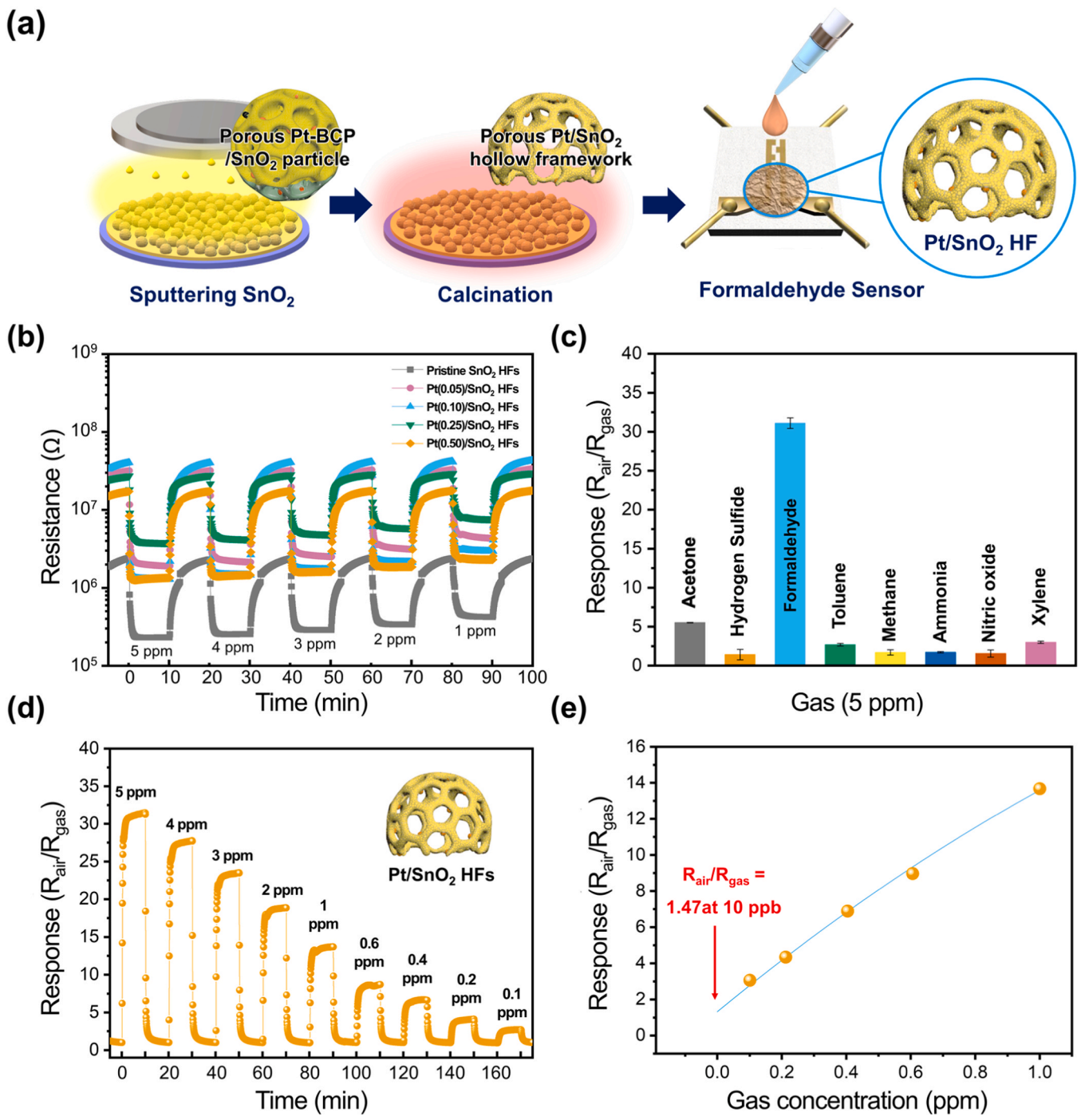

Fig. 4. HCHO sensing properties of Pt/SnO_2 HFs. (a) Schematic representation of sensor fabrication using Pt/SnO_2 HFs. (b) Responses of pristine SnO_2 HFs and Pt/SnO_2 HFs with various loading amounts (0.05, 0.10, 0.25, and 0.50 wt%) of Pt catalysts. The resistance transitions of all sensors are displayed in Fig. S9. (c) Selectivity of Pt(0.10)/SnO_2 HFs for the detection of HCHO against various analytes (acetone, hydrogen sulfide, formaldehyde, methane, ammonia, nitric oxide, and xylene). The concentration of analytes was controlled to 5 ppm. (d) Dynamic response transition of Pt(0.10)/SnO_2 HFs in the concentration range of 0.1−5.0 ppm of HCHO. (e) Linear approximation for the HCHO detection limit of Pt(0.10)/SnO_2 HFs. All sensing tests were conducted at 400 °C under dry air.

SnO_2. Therefore, there is an optimum loading amount for the Pt catalysts.

We further evaluated the selectivity of Pt(0.10)/SnO_2 HFs for HCHO detection. The Pt(0.10)/SnO_2 HFs exhibited high HCHO responses (31.4) compared to other interfering analytes (*i.e,* 5.6 for acetone [CH_3COCH_3], 1.4 for hydrogen sulfide [H_2S], 2.7 for toluene [$C_6H_5CH_3$], 1.7 for methane [CH_4], 1.6 for ammonia [NH_3], 1.6 for nitric oxide [NO], and 3.0 for xylene [$(CH_3)_2C_6H_4$]) (Fig. 4**c**). The response of the Pt(0.10)/SnO_2 HFs for HCHO was 5.6- to 22-fold higher than those to other gas molecules, highlighting the high selectivity of Pt/SnO_2 HFs for HCHO molecules. Noting that it is difficult to clearly define the origin of the high HCHO selectivity of Pt/SnO_2 HFs because the various factors can influence selectivity in metal oxide-based chemical gas sensors, such as operating temperatures [36], porosity and morphology [37], and the type and concentration of catalysts [38–40] (**Supporting Note 1**). However, numerous reports have demonstrated that SnO_2 with various catalysts exhibits high HCHO selectivity, as summarized in Table S1. In our case, the selectivity of Pt/SnO_2 HFs for

HCHO results from the intrinsic properties of SnO_2 combined with the catalytic enhancement provided by Pt NPs. In detail, the pristine SnO_2 HFs exhibited approximately 4-fold higher HCHO responses (10 for HCHO 5 ppm) compared to the highest responses to other interfering gases (2.5 for acetone at 5 ppm) (Fig. S11). However, after the decoration with Pt NPs on SnO_2 HFs, the HCHO responses of the sensors increased from 10.0 to 31.4, while the responses to acetone only increased from 2.5 to 5.6. As a result, the ratio of HCHO response to acetone response improves from 4.0 to 5.6 with the addition of Pt NPs, indicating that the Pt/SnO_2 HFs exhibited further improved HCHO selectivity than the pristine SnO_2 HFs. We also explored the detection limits of Pt(0.10)/SnO_2 HFs for HCHO sensing by evaluating the sensor responses to 0.1–5 ppm of HCHO (Fig. 4**d**). Pt(0.10)/SnO_2 HFs showed noticeable responses (3.06) even to HCHO 0.1 ppm. In addition, with linear approximation, the HCHO detection limit of Pt(0.10)/SnO_2 HFs was calculated to be 10 ppb with an estimated response of 1.47 (Fig. 4**e**). Compared to other SnO_2-based HCHO sensors [41–49], the Pt (0.10)/SnO_2 HFs exhibited fast sensing speed with ultra-low detection limits (Table S1). These sensing results reveal the potential of Pt (0.10)/SnO_2 HFs as highly effective sensors for HCHO detection.

In addition, to further support the selective detection of HCHO molecules, we applied a statistical analysis method that can facilitate machine learning using sensing data. We analyzed the raw data files stemming from sensor arrays using principal component analysis (PCA), a robust pattern recognition method tailored for large datasets. The sensor arrays consisted of SnO_2 HFs, Pt(0.05)/SnO_2 HFs, and Pt(0.10)/SnO_2 HFs, each associated with extensive datasets obtained from sensing measurements of diverse gas molecules. By subjecting our sensor array data to PCA, we enabled the recognition of patterns among various gas species. Fig. 5 shows the PCA analysis of the sensor arrays with three principal components. Notably, the sensing results for HCHO molecules are clustered in a distinct region amidst different gas molecules due to the high selectivity of Pt/SnO_2 HFs towards HCHO. Therefore, when the sensor arrays are exposed to HCHO gas molecules again, the PCA analysis of the additional data with the same principal components can show new points positioned within the HCHO region. Consequently, our sensors offer the capability to detect HCHO molecules through pattern recognition, potentially serving as components in machine learning-based intelligent gas sensing platforms.

Finally, we elucidate the sensing mechanism of Pt/SnO_2 HFs as follows. Typically, chemiresistive sensors based on metal oxides operate through surface reactions involving chemisorbed oxygen species (O^{2-} or O^-) and gas analytes [50]. The chemisorption of oxygen molecules from ambient air on the surface of SnO_2 leads to electron depletion in SnO_2 HFs. Subsequently, the surface reactions between chemisorbed oxygen species and HCHO molecules involve electron transfer to SnO_2 HFs, as described by the following equations (**Equations 1–3**) [51].

$$HCHO\ (gas) + 2O^{2-}\ (chemisorbed) \rightarrow CO_2\ (gas) + H_2O\ (gas) + 4e^- \quad (1)$$

$$HCHO\ (gas) + 2O^{-}\ (chemisorbed) \rightarrow CO_2\ (gas) + H_2O\ (gas) + 2e^- \quad (2)$$

$$HCHO\ (gas) + O^{-}\ (chemisorbed) \rightarrow CHOOH\ (gas) + e^- \quad (3)$$

The significant enhancement in the HCHO sensing properties of Pt/SnO_2 HFs is attributed to several key factors with their collective contributions. Firstly, the porous hollow structures of Pt/SnO_2 HFs play a pivotal role. These structures maximize the available reaction sites for gas molecules, enabling efficient gas-surface interactions. In addition, the hollow framework structure allows gas molecules to readily diffuse into the inner regions of Pt/SnO_2 HFs, substantially increasing the contact area of gas molecules with the sensing materials (Fig. 6**a**). This facilitates more chemical reactions between chemisorbed oxygen species and HCHO molecules on the surface of SnO_2 HFs, ultimately improving gas sensing performance. To demonstrate the effect of porous structure on sensing capabilities of our materials, we fabricated the SnO_2 films using the identical sputtering conditions employed for the preparation of SnO_2 HFs. We then evaluated the sensing performance of these SnO_2 films to HCHO molecules under the same operating conditions (5 ppm HCHO, dry, 400 °C) (Fig. S12). The SnO_2 thin films exhibited an ultra-low response (R_{air}/R_{gas} = 1.1) with a response time of 20 s, whereas those for the SnO_2 HF and Pt/SnO_2 HF were 10 (16 s) and 33 (4.7 s), respectively. It is noted that the response times of sensors are calculated by the time required to reach 90 % of the maximum response. Notably, the response and response speed of SnO_2 HFs were approximately 9.1-fold and 1.25-fold higher, respectively, compared to the SnO_2 thin films, demonstrating the effectiveness of the hollow structure in enhancing both the response speed and sensitivity of gas sensors.

Secondly, the catalytic effect of the tiny Pt NPs loaded on the Pt/SnO_2 HFs is also crucial in enhancing the sensor activity. Pt NPs, acted as catalysts [52], effectively reduce the activation energy required for surface reactions on SnO_2 HFs [41]. This reduction in activation energy promotes the chemisorption of oxygen species and their subsequent reactions with HCHO molecules. As a piece of evidence for the promotion of the chemisorption of oxygen species, the baseline resistance of Pt (0.10)/SnO_2 HFs (40 MΩ) is significantly higher than that of SnO_2 HFs (2.4 MΩ) (Fig. 6**b**). In addition, it is observed that the response speed increases with HCHO concentrations because the increased number of gas molecules reaching the surface of the sensors enhances the reaction kinetics ($r = k[HCHO_{(gas)}][O^-_{(ads)}]^2$) (Fig. 6**c**). It indicates that the response time is primarily influenced by reaction kinetics rather than gas diffusion, with a more pronounced effect in Pt-loaded SnO_2 HFs. Due to the catalyst effect of Pt NPs on surface reactions between HCHO and chemisorbed oxygen species, the resistance of Pt(0.10)/SnO_2 HFs was rapidly changed (4.7 s) with substantial changes (from 21.62 MΩ to 0.68 MΩ for 5 ppm HCHO). On the other hand, pristine SnO_2 HFs showed relatively sluggish response times (16 s) with low resistance changes (from 2.35 MΩ to 0.23 MΩ). This catalytic activation is more significant for the detection of low HCHO concentrations. In particular, Pt(0.10)/SnO_2 HFs require only 12 s to respond to 1 ppm of HCHO, whereas pristine SnO_2 HFs exhibit slower response times (56 s to HCHO 1 ppm) (Fig. 6**c**).

These sensing characteristics of Pt(0.10)/SnO_2 HFs comply with safety standards for HCHO exposure, aligning with the regulations of the California Division of Occupational Safety and Health (Cal/OSHA) in the United States. According to these regulations, the permissible exposure limits (PELs) for HCHO are 0.75 ppm for an 8-hour total weight average and 2 ppm for the short-term (15 min) PEL. Pt(0.10)/SnO_2 HFs meet

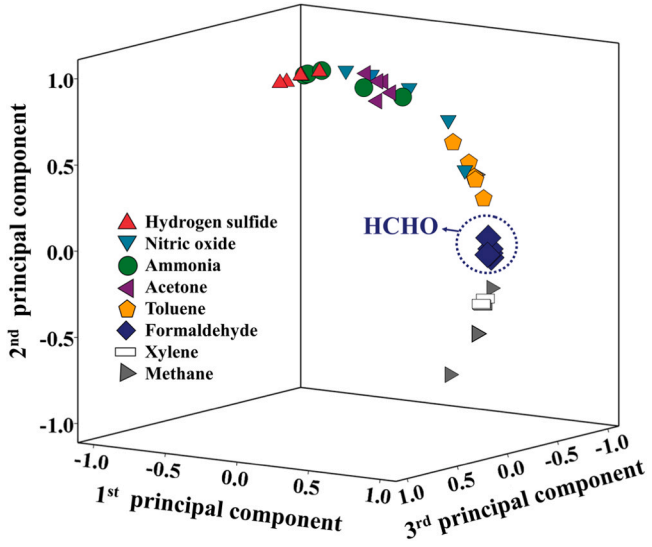

Fig. 5. Pattern recognition of various gas molecules. To obtain the patterns of gas molecules, the principal component analysis (PCA) was conducted using sensing results of SnO_2 HFs, Pt(0.05)/SnO_2 HFs, and Pt(0.10)/SnO_2 HFs.

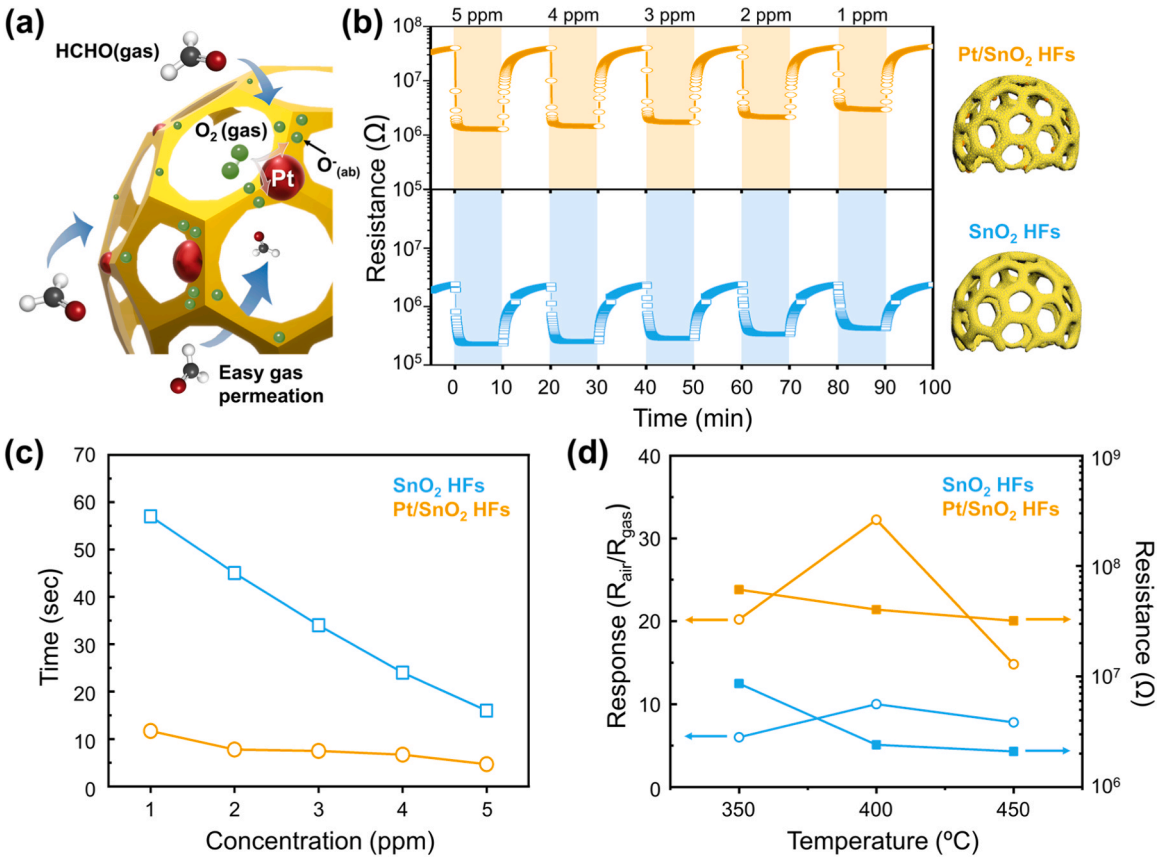

Fig. 6. Sensing mechanisms of Pt/SnO_2 HFs. (a) Schematic illustration of HCHO sensing mechanism for Pt/SnO_2 HFs and (b) dynamic resistance traces of SnO_2 HFs (bottom) and Pt(0.10)/SnO_2 HFs (top) in response to HCHO concentrations from 1 to 5 ppm. The operating temperature of the sensors was 400 °C under dry air, and the shaded area indicates the injection of HCHO gas molecules. (c) Response times of SnO_2 HFs and Pt(0.10)/SnO_2 HFs to 1–5 ppm of HCHO molecules. (d) Response and baseline resistance values of SnO_2 HFs and Pt(0.10)/SnO_2 HFs in response HCHO 5 ppm depending on operating temperatures (350, 400, and 450 °C) under dry air.

these safety standards, ensuring their suitability for practical applications. In addition, Pt(0.10)/SnO_2 HFs exhibited high responses even in a broad operating temperature range of 250–450 °C (Fig. 6**d and** Fig. S13), demonstrating Pt(0.10)/SnO_2 HFs are reliable HCHO sensors in diverse environmental conditions. Due to the increase of chemisorbed oxygen species, the baseline resistances (61 MΩ at 350 °C, 40 MΩ at 400 °C, and 32 MΩ at 450 °C) of Pt(0.10)/SnO_2 HFs in all measured operating temperatures were significantly higher than those (8.6 MΩ at 350 °C, 2.4 MΩ at 400 °C, and 2.0 MΩ at 450 °C) of SnO_2 HFs by a factor of 7–15 times, leading to a higher response of Pt(0.10)/SnO_2 HFs than SnO_2 HFs in a wide range of operating temperatures. It is noted that the slight decrease in baseline resistances of both sensors as increasing operating temperatures can be mainly attributed to the increase of major carriers in semiconductors [53], and the optimum sensing responses 400 °C indicated that the surface reactions between chemisorbed oxygen species and HCHO gas molecules in SnO_2 HFs and Pt/SnO_2 HFs are maximized at 400 °C.

4. Conclusions

In summary, this study focuses on the synthesis and development of Pt/SnO_2 HFs, a novel material that combines porous structures with catalytic NPs. The use of bicontinuous BCP microparticles with a porous framework plays a pivotal role in achieving a high surface area and enhanced gas permeability throughout the hollow structures, as well as in decorating well-dispersed Pt NPs. As a result, Pt/SnO_2 HFs exhibited exceptional sensing capabilities for HCHO, with high sensitivity, fast response, and low detection limit. In addition, Pt/SnO_2 HFs showed remarkable selectivity for HCHO detection, outperforming other interfering analytes. These sensing performances demonstrated that Pt/SnO_2 HFs are highly valuable for accurate and rapid detection of low concentrations of HCHO. Therefore, our approach to combining porous metal oxide hollow frameworks with nanoscopic catalysts can pave the way to achieve high-performance gas sensors for various applications, such as environmental monitoring, safety compliance, and health-related fields.

CRediT authorship contribution statement

Il-Doo Kim: Validation, Supervision, Resources, Project administration. **Kang Hee Ku:** Writing – review & editing, Supervision. **Sang-Joon Kim:** Writing – review & editing, Supervision, Formal analysis, Conceptualization. **Juyoung Lee:** Writing – review & editing, Methodology. **Hyunji Lee:** Writing – review & editing, Methodology. **Euichul Shin:** Writing – review & editing, Methodology. **Won-Tae Koo:** Writing – review & editing, Writing – original draft, Methodology, Formal analysis, Data curation. **Sungyoon Woo:** Writing – review & editing, Visualization, Methodology, Formal analysis, Data curation.

Declaration of Competing Interest

The authors declare no conflict of interest

Data Availability

Data will be made available on request.

Acknowledgments

This work was supported by the National Research Foundation of Korea (NRF) grant funded by the Korea government, Ministry of Science and ICT (Development of Ultra-High Density Nanofibers Yarn Based Multi-Modal Gas Sensor Platform) (2020R1A2C3013127); the STEAM BRIDGE R&D program (2022M3C1C3095083); and the Korean government (MSIT) (RS-2023-00259994 and 2022R1C1C1006324). This research was also supported by the Technology development Program (S3178295) funded by the Ministry of SMEs and Startups (MSS, Korea) and the Korea Technology and Information Promotion Agency for SMEs (Grant No. 00141845 and 00165289).

Appendix A. Supporting information

Supplementary data associated with this article can be found in the online version at doi:10.1016/j.snb.2024.136282.

References

[1] N.S. Ramgir, K. Sinju, B. Bhangare, A. Debnath, Electronic nose based on chemiresistive sensors for toxic gas detection, J. Mat. NanoSci. 9 (2022) 79–90.
[2] S.S. Shetty, A. Jayarama, I. Karunasagar, R. Pinto, A review on chemi-resistive human exhaled breath biosensors for early diagnosis of disease, Mat. Today.: Proc. 55 (2022) 122–126.
[3] W.-T. Koo, H.-J. Cho, D.-H. Kim, Y.H. Kim, H. Shin, R.M. Penner, et al., Chemiresistive hydrogen sensors: Fundamentals, recent advances, and challenges, ACS Nano 14 (2020) 14284–14322.
[4] M.A.A. Mamun, M.R. Yuce, Recent progress in nanomaterial enabled chemical sensors for wearable environmental monitoring applications, Adv. Funct. Mater. 30 (2020) 2005703.
[5] J. Tan, J. Xu, Applications of electronic nose (e-nose) and electronic tongue (e-tongue) in food quality-related properties determination: A review, Artif. Intell. Agric. 4 (2020) 104–115.
[6] R.J. Rath, S. Farajikhah, F. Oveissi, F. Dehghani, S. Naficy, Chemiresistive sensor arrays for gas/volatile organic compounds monitoring: A review, Adv. Eng. Mater. 25 (2023) 2200830.
[7] W.-T. Koo, J.-S. Jang, I.-D. Kim, Metal-organic frameworks for chemiresistive sensors, Chem 5 (2019) 1938–1963.
[8] M.A. Carpenter, S. Mathur, A. Kolmakov, Metal oxide nanomaterials for chemical sensors: Springer Science & Business Media; 2012.
[9] E. Comini, C. Baratto, I. Concina, G. Faglia, M. Falasconi, M. Ferroni, et al., Metal oxide nanoscience and nanotechnology for chemical sensors, Sens. Actuators, B Chem. 179 (2013) 3–20.
[10] L.-Y. Zhu, L.-X. Ou, L.-W. Mao, X.-Y. Wu, Y.-P. Liu, H.-L. Lu, Advances in Noble Metal-decorated metal oxide nanomaterials for chemiresistive gas sensors: Overview, Nano-Micro Lett. 15 (2023) 89.
[11] B. Choi, D. Shin, H.-S. Lee, H. Song, Nanoparticle design and assembly for p-type metal oxide gas sensors, Nanoscale 14 (2022) 3387–3397.
[12] M.E. Franke, T.J. Koplin, U. Simon, Metal and metal oxide nanoparticles in chemiresistors: Does the nanoscale matter? Small 2 (2006) 36–50.
[13] J. Lin, M. Kilani, G. Mao, Recent advances in integrating 1D nanomaterials into chemiresistive gas sensor devices, Adv. Mater. Technol. 8 (2023) 2202038.
[14] B. Yang, N.V. Myung, T.T. Tran, 1D metal oxide semiconductor materials for chemiresistive gas sensors: A review, Adv. Electron. Mater. 7 (2021) 2100271.
[15] A.P. Dral, J.E. ten Elshof, 2D metal oxide nanoflakes for sensing applications: Review and perspective, Sens. Actuators, B Chem. 272 (2018) 369–392.
[16] B. Mondal, P.K. Gogoi, Nanoscale heterostructured materials based on metal oxides for a chemiresistive gas sensor, ACS Appl. Electron. Mater. 4 (2022) 59–86.
[17] N. Chowdhury, B. Bhowmik, Micro/nanostructured gas sensors: the physics behind the nanostructure growth, sensing and selectivity mechanisms, Nanoscale Adv. 3 (2021) 73–93.
[18] Y. Kong, Y. Li, X. Cui, L. Su, D. Ma, T. Lai, et al., SnO_2 nanostructured materials used as gas sensors for the detection of hazardous and flammable gases: A review, Nano Mater. Sci. 4 (2022) 339–350.
[19] C. Zhu, D. Du, A. Eychmüller, Y. Lin, Engineering ordered and nonordered porous noble metal nanostructures: synthesis, assembly, and their applications in electrochemistry, Chem. Rev. 115 (2015) 8896–8943.
[20] K.H. Ku, J.M. Shin, M.P. Kim, C.-H. Lee, M.-K. Seo, G.-R. Yi, et al., Size-controlled nanoparticle-guided assembly of block copolymers for convex lens-shaped particles, J. Am. Chem. Soc. 136 (2014) 9982–9989.
[21] N. Yan, X. Liu, J. Zhu, Y. Zhu, W. Jiang, Well-ordered inorganic nanoparticle arrays directed by block copolymer nanosheets, ACS Nano 13 (2019) 6638–6646.
[22] T. Kim, M. Xu, Y.J. Lee, K.H. Ku, D.J. Shin, D.C. Lee, et al., Fluorescence switchable block copolymer particles with doubly alternate-layered nanoparticle arrays, Small 17 (2021) 2101222.
[23] A. Kaur, B. Bajaj, A. Kaushik, A. Saini, D. Sud, A review on template assisted synthesis of multi-functional metal oxide nanostructures: Status and prospects, Mater. Sci. Eng.: B 286 (2022) 116005.
[24] M. Li, C.K. Ober, Block copolymer patterns and templates, Mater. Today 9 (2006) 30–39.
[25] B. Smarsly, M. Antonietti, Block copolymer assemblies as templates for the generation of mesoporous inorganic materials and crystalline films, Eur. J. Inorg. Chem. 2006 (2006) 1111–1119.
[26] J. Zhu, R.C. Hayward, Hierarchically structured microparticles formed by interfacial instabilities of emulsion droplets containing amphiphilic block copolymers, Angew. Chem. Int. Ed. 120 (2008) 2143–2146.
[27] K.H. Ku, J.M. Shin, D. Klinger, S.G. Jang, R.C. Hayward, C.J. Hawker, et al., Particles with tunable porosity and morphology by controlling interfacial instability in block copolymer emulsions, ACS Nano 10 (2016) 5243–5251.
[28] S. Liu, Y. Dong, W. Zhang, L. Hu, C. Li, Z. Meng, et al., Porous polymer particles with tunable surface roughness by combining phase separation and interfacial instability, ACS Appl. Polym. Mater. 5 (2023) 1103–1108.
[29] J.M. Shin, M.P. Kim, H. Yang, K.H. Ku, S.G. Jang, K.H. Youm, et al., Monodipserse nanostructured spheres of block copolymers and nanoparticles via cross-flow membrane emulsification, Chem. Mater. 27 (2015) 6314–6321.
[30] J.M. Shin, Y.J. Lee, M. Kim, K.H. Ku, J. Lee, Y. Kim, et al., Development of shape-tuned, monodisperse block copolymer particles through solvent-mediated particle restructuring, Chem. Mater. 31 (2019) 1066–1074.
[31] D. McNulty, H. Geaney, Q. Ramasse, C. O'Dwyer, Long cycle life, highly ordered SnO_2/GeO_2 nanocomposite inverse opal anode materials for Li-ion batteries, Adv. Funct. Mater. 30 (2020) 2005073.
[32] S.J. Kim, S.J. Choi, J.S. Jang, H.J. Cho, W.T. Koo, H.L. Tuller, et al., Exceptional high-performance of Pt-based bimetallic catalysts for exclusive detection of exhaled biomarkers, Adv. Mater. 29 (2017) 1700737.
[33] S. Porsgaard, L.R. Merte, L.K. Ono, F. Behafarid, J. Matos, et al., Stability of platinum nanoparticles supported on SiO_2/Si(111): A high-pressure X-ray photoelectron spectroscopy study, ACS Nano 6 (2012) 10743–10749.
[34] L.K. Ono, J.R. Croy, H. Heinrich, B.R. Cuenya, Oxygen chemisorption, formation, and thermal stability of Pt oxides on Pt nanoparticles supported on SiO_2/Si(001): Size effects, J. Phys. Chem. C. 115 (2011) 16856–16866.
[35] Y.J. Jeong, D.-H. Kim, J.-S. Jang, J.-Y. Kang, R. Kim, I.-D. Kim, Bio-inspired heterogeneous sensitization of bimetal oxides on SnO_2 scaffolds for unparalleled formaldehyde detection, Chem. Commun. 55 (2019) 3622–3625.
[36] Z. Jing, J. Zhan, Fabrication and gas-sensing properties of porous ZnO nanoplates, Adv. Mater. 20 (2008) 4547–4551.
[37] T. Kida, et al., Pore and particle size control of gas sensing films using SnO_2 nanoparticles synthesized by seed-mediated growth: design of highly sensitive gas sensors, J. Phys. Chem. C. 117 (2013) 17574–17582.
[38] S.-J. Choi, et al., Selective diagnosis of diabetes using Pt-functionalized WO_3 hemitube networks as a sensing layer of acetone in exhaled breath, Anal. Chem. 85 (2013) 1792–1796.
[39] N.-H. Kim, et al., Highly sensitive and selective hydrogen sulfide and toluene sensors using Pd functionalized WO_3 nanofibers for potential diagnosis of halitosis and lung cancer, Sens. Actuators, B Chem. 193 (2014) 574–581.
[40] J.-K. Choi, et al., Design of selective gas sensors using electrospun Pd-doped SnO_2 hollow nanofibers, Sens. Actuators, B Chem. 150 (2010) 191–199.
[41] Y. Tang, Z. Han, Y. Qi, Z. Yang, H. Han, Y. Jiang, et al., Enhanced ppb-level formaldehyde sensing performance over Pt deposited SnO_2, nanospheres, J. Alloy. Compd. 899 (2022) 163230.
[42] X. Zhu, X. Zhang, X. Chang, J. Li, L. Pan, Y. Jiang, et al., Metal-organic framework-derived porous SnO_2 nanosheets with grain sizes comparable to Debye length for formaldehyde detection with high response and low detection limit, Sens. Actuators, B Chem. 347 (2021) 130599.
[43] Z. Yang, W. Cao, C. Peng, T. Wang, B. Li, H. Ma, et al., Construction, application and verification of a novel formaldehyde gas sensor system based on Ni-doped SnO_2 nanoparticles, IEEE Sens. J. 21 (2021) 11023–11030.
[44] D. Sun, X. Tang, S. Li, L. Liu, Yb-doped 3D ordered porous SnO_2 with a controllable pore size for ppb level formaldehyde detection, IEEE Sens. J. 21 (2021) 18271–18278.
[45] D. Sun, X. Tang, S. Li, L. Liu, Ga-doped 3D ordered porous SnO_2 for enhanced formaldehyde sensing performance, J. Phys. Chem. C. 125 (2021) 11107–11114.
[46] C. Lou, Q. Huang, Z. Li, G. Lei, X. Liu, J. Zhang, Fe_2O_3-sensitized SnO_2 nanosheets via atomic layer deposition for sensitive formaldehyde detection, Sens. Actuators, B Chem. 345 (2021) 130429.
[47] Z.-L. Chen, D. Wang, X.-Y. Wang, J.-H. Yang, Enhanced formaldehyde sensitivity of two-dimensional mesoporous SnO_2 by nitrogen-doped graphene quantum dots, Rare Met. 40 (2021) 1561–1570.
[48] Y. Zhao, H. Li, Y. Li, Y. Ma, H. Yang, H. Liu, et al., Layered SnO_2 nanorods arrays anchored on reduced graphene oxide for ultra-high and ppb level formaldehyde sensing, Sens. Actuators, B Chem. 346 (2021) 130452.
[49] S. Zhou, H. Wang, J. Hu, T. Lv, Q. Rong, Y. Zhang, et al., Formaldehyde gas sensor with extremely high response employing cobalt-doped SnO_2 ultrafine nanoparticles, Nanoscale Adv. 4 (2022) 824–836.
[50] S. Das, S. Mojumder, D. Saha, M. Pal, Influence of major parameters on the sensing mechanism of semiconductor metal oxide based chemiresistive gas sensors: A review focused on personalized healthcare, Sens. Actuators, B Chem. 352 (2022) 131066.
[51] Y. Cao, X. Zou, Y. He, G.-D. Li, Sens. Actuators, B Chem. 252 (2017) 232–238.
[52] W.-T. Koo, Y. Kim, S. Kim, B.L. Suh, S. Savagatrup, J. Kim, et al., Hydrogen sensors from composites of ultra-small bimetallic nanoparticles and porous ion-exchange polymers, Chem 6 (2020) 2746–2758.
[53] I.-D. Kim, A. Rothschild, H.L. Tuller, Advances and new directions in gas-sensing devices, Acta Mater. 61 (2013) 974–1000.

Won-Tae Koo received his BS degree in Materials Science and Engineering at Hanyang University. He also obtained both his MS and PhD degrees in in Materials Science and Engineering at Korea Advanced Institute of Science and Technology.

Sungyoon Woo received his BS degree in Materials Science and Engineering at Hanyang University. He also obtained his MS in in Materials Science and Engineering at Korea Advanced Institute of Science and Technology.

Euichul Shin received his BS degree in Materials Science and Engineering at Hanyang University. He also obtained his MS in in Materials Science and Engineering at Korea Advanced Institute of Science and Technology.

Juyoung Lee graduated with a BS in Chemical Engineering from Chungnam National University. He is now pursuing a combined MS/PhD program in the School of Energy and Chemical Engineering at UNIST, under the guidance of Prof. Kang Hee Ku.

Hyunji Lee obtained her bachelor's degree in Chemical and Biological Engineering from Hanbat University. Following that, she completed an internship at the CO2 Energy Research Center at KRICT. Presently, she is pursuing her Master's degree in Advanced Materials and Chemical Engineering at UST.

Kang Hee Ku is currently serving as an assistant professor in the School of Energy and Chemical Engineering at UNIST. She received her PhD degree from KAIST in Chemical and Biomolecular Engineering under the guidance of Prof. Bumjoon Kim. She later worked with Prof. Timothy M. Swager at MIT as a postdoctoral researcher.

Sang-Joon Kim earned his PhD in Materials Science and Engineering (MSE) from KAIST. Subsequently, he served as a Senior Scientist at SK Hynix and pursued his postdoctoral research at MIT under the mentorship of Prof. Harry H. Tuller. Currently, Dr. Kim holds the position of Senior Research Scientist at the CO2 & Energy Research Center at KRICT in the Republic of Korea. In addition to his research role, he serves as an Associate Professor at UST.

Il-Doo Kim received his PhD degree in Materials Science and Engineering from KAIST. He later worked at Massachusetts Institute of Technology as a Postdoctoral Fellow under Prof. Harry H. Tuller. Currently, Dr. Kim works as Professor in the Department of Materials Science and Engineering at KAIST in Republic of Korea. Also, He is executive editor of ACS Nano.